Convective Heat and Mass Transfer to a Cylinder Sheathed by a Porous Layer

Michal P. Sobera, Chris R. Kleijn, and Harry E. A. Van den Akker
Kramers Laboratorium voor Fysische Technologie, Delft University of Technology,
2628 BW Delft, The Netherlands

Paul Brasser
TNO Prins Maurits Laboratory, 2280 AA Rijswijk, The Netherlands

A systematic study of the flow, heat, and mass transfer around a cylinder sheathed by a second, porous cylinder and placed in a perpendicular turbulent air flow has been performed. The focus of the study was on applications in heat and mass transfer to a clothed human limb in outdoor conditions. Both numerical and experimental investigations have been carried out for the fluid flow. Dimensionless scaling rules have been presented for flow, heat and mass transfer as a function of the free stream Reynolds number, the Darcy number, the dimensionless air resistance of the porous layer, and the dimensionless distance between the outer and inner cylinder. The results have been compared to available data in the literature and to the present experiment. An empirical correlation, which concludes the most important results, has been proposed. The largest reduction of heat and mass transfer due to the sheath layer, compared to that for an uncovered cylinder, was found for intermediate values of the Reynolds number, the flow resistance of the sheath layer, and the thickness of the air gap between solid and sheath cylinder.

Introduction

Because of their large technological relevance in, for instance, chemical engineering and energy conversion, heat and mass transfer to circular cylinders exposed to a turbulent fluid flow have been widely studied. Accurate empirical correlations are available for Nusselt and Sherwood numbers as a function of free stream Reynolds number and turbulence intensity (Zdravkovich, 1997; Bird et al., 2002; Sanitjai and Goldstein, 2001). Accurate numerical predictions of the turbulent flow around and the heat and mass transfer to circular cylinders have become possible in the last decade, using, for example, Reynolds averaged Navier-Stokes equations (RANS) (Celik and Shafer, 1995) or large eddy simulations (LES) (Breuer, 1998). For applications in, for example, ground water flow and heat and mass transfer inside fixed-bed reactors, the heat and mass transfer to a cylinder embedded in a porous medium through which a fluid is flowing has been studied (for example, Haddad et al., 2001; Thevenin, 1995).

Correspondence concerning this article should be addressed to C. R. Kleijn.

A configuration that has received relatively little attention is that of a cylinder surrounded at some distance by a second, larger, porous cylinder (see Figure 1a). Applications can be found in, for example, filtering and separation technology, but the most important application is probably that of human clothing. A cylinder covered at some distance by a layer of fabric is widely used as a standard model configuration for a human limb, to study the comfort and protection offered by various types of clothing. An experimental study of the velocity field around a fabric-covered cylinder has been reported by Watanabe et al. (1991). They studied the influence of the porous-layer permeability on the velocity of the flow underneath the porous layer. Experimental results on heat transfer to a fabric-covered cylinder have been reported by Kind et al. (1995). Gibson (1999) presented numerical computations of the air flow and heat transfer to a fabric-covered cylinder. A numerical study of free and mixed convection around a cylinder surrounded by porous material, focusing on thermal comfort in situations were there is no or very little external air

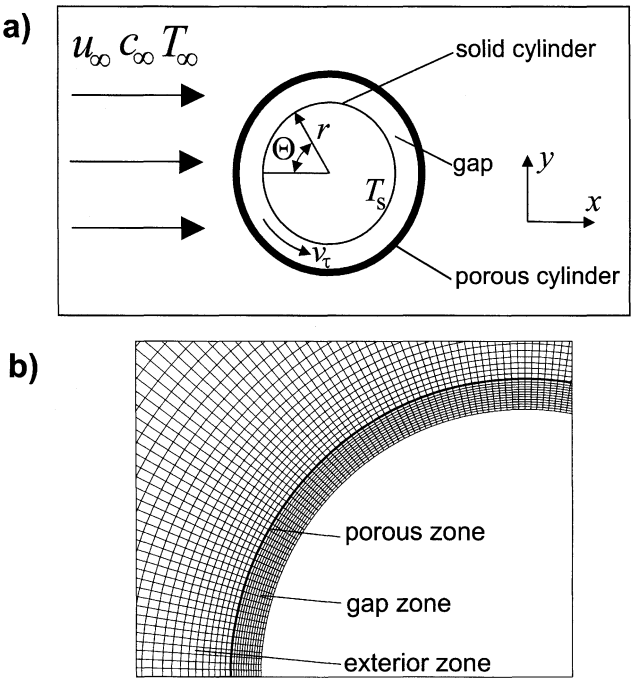

Figure 1. (a) Problem description and (b) a fragment of computational domain.

flow, was presented by Bo and Nakijama (2001). A general overview of numerical modeling dedicated to protective clothing has been reported by Gibson (1999), who outlined the model equations describing coupled heat and mass transfer through a hygroscopic porous material. An experimental study on the thermal insulation of garments has been reported by Bouskill et al. (2002). Holmer et al. (1999) presented improvements in experimental predictions of the convective heat transfer, with an application to clothing.

At present, no systematic study of the heat and mass transfer to a cylinder sheathed by a porous layer, as a function of all the relevant parameters, has been performed. In this article, we present such a systematic study, based on computational fluid dynamics and experimental validation, and we address the question of to what extent heat and mass transfer characteristics are altered by the porous sheath. Although we focus on application to the system of a human limb covered by a layer of clothing, the problem is formulated in a general manner and valid for many other applications. The geometry studied is shown in Figure 1. The solid (inner) cylinder might represent a human limb, and the surrounding porous layer (outer cylinder) could represent a layer of clothing material. The space in between both cylinders is filled with air. The system is placed in an external, uniform, turbulent air flow. The focus is on situations with significant outer air flow, such that natural convection can be neglected.

In the following sections, some general theory on turbulent flow around a cylinder is presented, followed by the governing model equations and dimensionless numbers. Then, the numerical details are shown. A subsequent section describes the experimental setup. Finally, numerical and experimental results are presented and discussed.

Theory

Flow around a solid cylinder

Flow around a solid circular cylinder is characterized by the Reynolds number $Re = (\rho u_\infty D)/\mu$ (for a list of used symbols, see the Notation Section). In the range of $Re = 10^3$ to 10^7, the flow is periodic and transitional in character. Periodicity of the flow is due to the vortex shedding at the cylinder surface. Different flow patterns can be identified, for which various terminology has been proposed by different authors. In the present work, the terminology proposed by Zdravkovich (1997) has been used, where the flow is divided into subcritical, critical, and fully turbulent regimes. Each regime is marked by different behavior of the boundary layer, and is characterized by the drag coefficient c_D and dimensionless frequency of vortex shedding (Strouhal number: $St = (fD)/u_\infty$). In the subcritical flow regime ($10^3 \le Re \le 10^5$), the boundary layer remains fully laminar up to the separation point, and the drag coefficient and St remain almost constant ($c_D = 1$ to 1.2, $St \approx 0.20$). In the critical flow regime ($10^5 \le Re \le 10^7$), characterized by the so-called drag crisis, transition occurs in the boundary layer, starting at the separation point. St increases up to about 0.5. The transition region advances asymptotically toward the stagnation point with an increasing Reynolds number. The fully turbulent regime is reached when all of the flow regions around the cylinder are turbulent ($Re > 10^7$). In the present article, flows in the subcritical flow regime have been considered ($3.5 \cdot 10^3 \le Re \le 3.5 \cdot 10^4$).

Model equations

The fluid flow in the geometry studied can be described by a set of partial differential equations (White, 1991). For an incompressible fluid, the mass conservation (continuity) equation is expressed as

$$\nabla \cdot \boldsymbol{V} = 0 \tag{1}$$

Assuming that buoyancy effects are negligible, the momentum equation can then be written as

$$\rho \frac{\partial}{\partial t}\boldsymbol{V} + \rho(\nabla \cdot \boldsymbol{V}\boldsymbol{V}) = -\nabla P + \nabla \cdot \bar{\bar{\tau}} - \alpha \boldsymbol{S} \tag{2}$$

where $\bar{\bar{\tau}}$ is the viscous stress tensor, that is

$$\bar{\bar{\tau}} = \mu\left(\nabla \boldsymbol{V} + (\nabla \boldsymbol{V})^\dagger\right) \tag{3}$$

$(\cdot)^\dagger$ denotes a transposed vector, α is a binary parameter, with

$$\alpha = \begin{cases} 1 & \text{in the porous region} \\ 0 & \text{in the fluid region} \end{cases}$$

and $\boldsymbol{S}$ describes the momentum source term vector in the porous zone. It is written in accordance with Darcy's law and given by

$$\boldsymbol{S} = \frac{\mu}{K}\boldsymbol{V} \tag{4}$$

When the thickness δ_c of the porous layer is very small, this layer can be treated as a thin flow resistance, causing a discrete pressure drop

$$\Delta P = \frac{\mu \delta_c}{K} V \tag{5}$$

Additionally, the equations of heat and mass transfer have been considered. The heat-transfer equation is given by

$$\rho c_p \frac{\partial T}{\partial t} + \rho c_p (V \cdot \nabla T) = \lambda \nabla^2 T \tag{6}$$

and in a similar way, the species transport equation for tracer gas present in the air in small concentration is

$$\frac{\partial c}{\partial t} + V \cdot \nabla c = \mathfrak{D} \nabla^2 c \tag{7}$$

In the preceding, it has been assumed that the gas properties ρ, μ, λ, and c_p are constant. In our study, it has been assumed that heat and mass transfer through the porous material are dominated by convection with the flowing air. Solid heat conduction and mass diffusion in the clothing material have been neglected. It has also been assumed that the air flow in the gap between the solid inner and porous outer cylinder is laminar. Based on a typical air velocity of 0.5 m/s and a typical gap height of 5 mm, the Reynolds number for this air flow is of the order 100.

The flow around the outer cylinder, however, is turbulent. For the prediction of this flow at the Reynolds numbers of interest, direct numerical simulations (DNS), and even LES, are computationally very intensive. Therefore, using the RANS approach to turbulence modeling is attractive. However, with RANS turbulence models, an accurate prediction of the outer flow around a cylinder is difficult to achieve for the relevant range of Reynolds numbers ($3.5 \cdot 10^3 \div 3.5 \cdot 10^4$). Therefore, special attention has been paid to the accuracy of used RANS turbulence models for predicting the flow around an uncovered (bare) cylinder. This is described below.

Dimensionless model equations

Assuming constant air properties, Eqs. 1–7 can be made dimensionless by introducing the following dimensionless parameters

$$\hat{V} = \frac{V}{u_\infty} \qquad \hat{c} = \frac{c}{c_\infty} \qquad \hat{T} = \frac{T - T_\infty}{T_s - T_\infty}$$

$$\hat{P} = \frac{P}{\rho u_\infty^2} \qquad \hat{t} = \frac{u_\infty}{D} t \qquad \hat{\nabla} = \nabla D \tag{8}$$

Here, u_∞ is the free stream velocity, c_∞ is the free stream concentration of the trace gas, T_∞ is the free stream air temperature, T_s is the surface temperature of the inner cylinder, and D is the characteristic length, taken to be the diameter of the outer cylinder for cases in which a covered cylinder is studied, and as the diameter of the cylinder itself in cases in which an uncovered cylinder is studied. This leads to equations in dimensionless form as below

(1) Continuity equation

$$\hat{\nabla} \cdot \hat{V} = 0 \tag{9}$$

(2) Momentum equation

$$\frac{\partial \hat{V}}{\partial \hat{t}} + \hat{\nabla} \cdot \hat{V}\hat{V} = -\hat{\nabla}\hat{P} + \frac{1}{Re} \hat{\nabla} \cdot \left[\hat{\nabla}\hat{V} + \left(\hat{\nabla}\hat{V} \right)^\dagger \right] - \alpha \frac{1}{Ic^2 DaRe} \hat{V} \tag{10}$$

(3) Heat-transfer equation

$$\frac{\partial \hat{T}}{\partial \hat{t}} + \hat{V} \cdot \hat{\nabla}\hat{T} = -\frac{1}{RePr} \hat{\nabla}^2 \hat{T} \tag{11}$$

(4) Species transport equation

$$\frac{\partial \hat{c}}{\partial \hat{t}} + \hat{V} \cdot \hat{\nabla}\hat{c} = -\frac{1}{ReSc} \hat{\nabla}^2 \hat{c} \tag{12}$$

The last term on the righthand side of Eq. 10 is felt in the porous layer only, which has dimensionless thickness Ic. The total impact on the momentum balance will therefore scale with $Ic \cdot (ReDaIc^2)^{-1} = (ReDaIc)^{-1}$. This also can be understood by putting Eq. 5 in dimensionless form, leading to

$$\frac{\Delta \hat{P}}{\hat{V}} = \frac{1}{ReDaIc} \tag{13}$$

It is now clear that in the preceding equations four independent dimensionless groups appear: Re, Sc, Pr, and $DaIc$. Together with the surface Damköhler number (Da_s), which will appear through the boundary conditions (see below), and the geometric parameter $Ig = \delta_g/D$, they give a complete description of the problem.

Turbulence models

Two different two-equation k-ϵ eddy viscosity turbulence models were studied. Here, turbulence is modeled by replacing the molecular viscosity in the steady-state momentum equation by an eddy or turbulent viscosity, which is calculated from the turbulent kinetic energy k and turbulence dissipation rate ϵ. Similarly, in the averaged heat and species transport equation, the molecular thermal conductivity and diffusivity are replaced by an eddy thermal conductivity and diffusivity. Two additional transport equations are solved for k and ϵ.

In the standard k-ϵ model (Ferziger and Peric, 1996) these equations are

$$\rho (V \cdot \nabla k) = \nabla \cdot \left[\left(\mu + \frac{\mu_t}{\sigma_k} \right) \nabla k \right] + G_k - \rho \epsilon \tag{14}$$

$$\rho (V \cdot \nabla \epsilon) = \nabla \cdot \left[\left(\mu + \frac{\mu_t}{\sigma_\epsilon} \right) \nabla \epsilon \right] + C_{1\epsilon} \frac{\epsilon}{k} G_k - C_{2\epsilon} \rho \frac{\epsilon^2}{k} \tag{15}$$

where G_k is the production rate of turbulent kinetic energy due to the mean shear. The model constants have the following values: $C_{1\epsilon} = 1.44$, $C_{2\epsilon} = 1.92$, $\sigma_k = 1.0$, $\sigma_\epsilon = 1.3$. The turbulent viscosity is calculated as

$$\mu_t = C_\mu \rho \frac{k^2}{\epsilon} \tag{16}$$

with $C_\mu = 0.09$.

Because of known weaknesses of the standard k-ϵ model in predicting flows around cylinders (Casey and Wintergerste, 2000), another version was also considered, namely, the RNG k-ϵ model, which was derived from instantaneous Navier-Stokes equations by using a mathematical technique called renormalization group theory (Fluent Inc., 1998). In the RNG k-ϵ model, the transport equations for k and ϵ are

$$\rho(V \cdot \nabla k) = \nabla \cdot (\alpha_k \mu_{\text{eff}} \nabla k) + G_k - \rho\epsilon \tag{17}$$

$$\rho(V \cdot \nabla \epsilon) = \nabla \cdot (\alpha_\epsilon \mu_{\text{eff}} \nabla \epsilon) + C_{1\epsilon} \frac{\epsilon}{k} G_k - C_{2\epsilon} \rho \frac{\epsilon^2}{k} \tag{18}$$

with $\mu_{\text{eff}} = \mu + \mu_t$. The model constants now have the following values: $C_{1\epsilon} = 1.42$, $C_{2\epsilon} = 1.68$, $\alpha_k = \alpha_\epsilon = 1.393$. The RNG theory provides a differential formula for the effective viscosity that accounts for low-Reynolds number effects. In the high Re limit, the turbulent diffusivity is again calculated from Eq. 16, but with a value $C_\mu = 0.0845$. The RNG k-ϵ model is expected to give better predictions of the flow around a cylinder for the Re range considered in the present study (Casey and Wintergerste, 2000).

Numerical Model

The preceding set of differential equations with boundary conditions has been solved by use of the CFD code Fluent 5 (Fluent Inc., 1998). Computations were based on the finite volume formulation, employing the second-order upwind spatial discretization and the well-known SIMPLE pressure-velocity coupling algorithm (Patankar, 1980).

Two different computational meshes have been used for solving the flow around the bare and the porous covered cylinder, respectively. Both are two-dimensional (2-D) cylindrical grids with approximately $1.5 \cdot 10^4$ cells. Based on the symmetry of the time-averaged flow, only half of the physical domain has been considered. For the covered case, the computational domain consists of three separate zones: the external air-flow zone, the porous-medium zone, and the air-gap zone between the inner and outer cylinder (Figure 1b). There were 20 radial grid cells in the air-gap zone and 2 radial grid cells in the porous-layer zone. There were 280 grid cells in the angular direction. Because of the relatively low velocity inside the air gap, the inner flow was assumed to be laminar, whereas the outer flow was assumed to be turbulent. The grid for the uncovered cylinder was based on the one used by Celik and Shafer (1995). For both situations, solutions were checked for grid independence by refinement by a factor of 2 in the radial and angular directions.

For the bare cylinder, only calculations of the flow field were performed. At the inlet, a constant horizontal velocity was specified, as well as a turbulence intensity, $I_t = 4\%$, and a turbulence length scale, $L_t = 1D$. By varying I_t between 2% and 8% and L_t between $0.5D$ and $2D$, it was checked that the solutions were virtually independent of the selected turbulence inflow parameters. On the surface of the cylinder, standard wall functions for velocity, k and ϵ were prescribed. The other boundaries of the domain were defined as free outlets.

Table 1. Boundary Conditions for Fluid Flow, Heat, and Mass-Transfer Calculations

Inlet Boundary Conditions	Surface Boundary Conditions
$V_x = u_\infty \rightarrow \hat{V}_x = 1$ $V_y = 0 \rightarrow \hat{V}_y = 0$ $v' = \frac{u_\infty}{25} \rightarrow \hat{v}' = 0.04$	$V = 0 \rightarrow \hat{V} = 0$
$T = T_\infty \rightarrow \hat{T} = 0$	$T = T_s \rightarrow \hat{T} = 1$
$c = c_\infty \rightarrow \hat{c} = 1$	$\mathfrak{D}\frac{\partial c}{\partial n} = k_a c_\infty \rightarrow \frac{\partial \hat{c}}{\partial \hat{n}} = Da_s \hat{c}$

For the case of a cylinder sheathed by a second porous cylinder, heat and mass transfer also have been computed. A uniform temperature and trace gas concentration have been specified at the inlet (see Table 1). A constant temperature has been assumed at the surface of the inner cylinder. Since the flow in the air gap was assumed to be laminar, a simple no-slip boundary condition without a turbulence wall function was used on the inner cylinder surface. The porous sheath was treated as a fluid zone, where the pressure drop was imposed. Thus, no boundary conditions had to be imposed on the inner and outer interface of the porous sheath layer. It was assumed that the tracer gas adsorbs on the inner cylinder wall through a linear adsorption process, with rate $R = k_a c$. For $k_a \rightarrow 0$, this corresponds to a zero-flux Neumann boundary condition on the inner cylinder wall, whereas for $k_a \rightarrow \infty$, it corresponds to a $c = 0$ Dirichlet boundary condition. In dimensionless form, this adsorptivity appears in the Damköhler number Da_s, defined in Table 2.

Experimental Studies

This section presents the experimental setup used for laser doppler anemometry (LDA) measurements of the flow field for validating the numerical flow computations.

Table 2. The Set of Dimensionless Parameters

Dimensionless Group	Definition
Reynolds number (Re)	$Re = \frac{\rho u_\infty D}{\mu}$
Darcy number (Da)	$Da = \frac{K}{\delta_c^2}$
Damköhler number (Da_s)	$Da_s = \frac{k_a \delta_g}{\mathfrak{D}}$
Prandtl number (Pr)	$Pr = \frac{\mu c_p}{\lambda}$
Schmidt number (Sc)	$Sc = \frac{\mu \rho}{\mathfrak{D}}$
Porous thickness ratio (Ic)	$Ic = \frac{\delta_c}{D}$
Air gap thickness ratio (Ig)	$Ig = \frac{\delta_g}{D}$

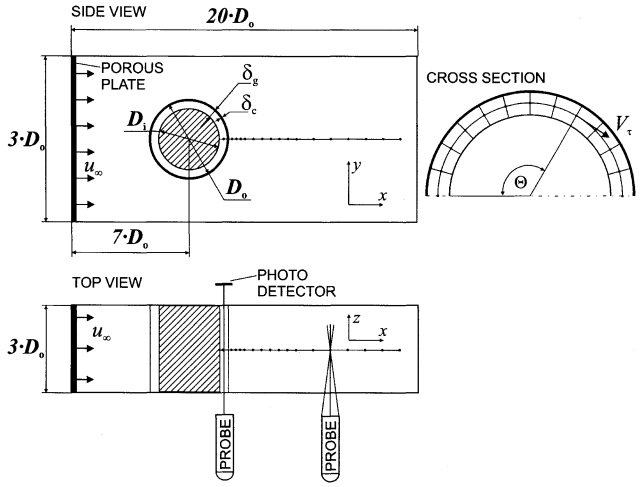

Figure 2. Experimental setup configuration with measurement grid for bare cylinder (left part) and covered cylinder (right part).

The experimental section is presented in Figure 2. The main part of the measuring section consists of a Plexiglas water tunnel with a square cross section of 0.15 m × 0.15 m and a length of 1 m. In the water tunnel, a cylinder with a diameter of $D_i = 0.036$ m and a length of $L = 0.15$ m is placed perpendicular to the water flow direction. This cylinder may be covered by a layer of textile material at a distance of $\delta_g = 0.005$ m from the inner cylinder surface. Thus, the blockage ratio, b, defined as the ratio of the tunnel height over the cylinder diameter ($b = H/D$), was $b \approx 4.2$ for the uncovered and $b \approx 3.3$ for the covered case. Also the aspect ratios (L/D) were $L/D \approx 4.2$ and $L/D \approx 3.3$, respectively. The maximum velocity inside the water tunnel was slightly above 1 m/s. This corresponds to $Re = 5 \cdot 10^4$ (based on the diameter of the outer cylinder), and covers the range of interest. In order to obtain a uniform velocity profile inside the tunnel, a porous plate of metal foam was used as a flow straightener at the inlet of the section. Directly behind this plate, the time-averaged free-stream velocity across the channel was found to be uniform within 2%, and the turbulence intensity was 3–4%. The relatively small values of b and L/D can cause a local increase of Re. Nevertheless, the flow stays in the subcritical regime and the dimensionless pressure distribution around the porous cylinder remains unaffected. As a consequence, the dimensionless velocity inside the air gap stays the same, as confirmed by numerical simulations.

The experimental work was divided into two parts: the first dealt with the flow around a bare cylinder, and the second with the flow in the gap between a solid inner cylinder and its porous cover.

The experiments for the bare cylinder were performed to test the experimental facility and to validate the computations and in particular the used turbulence models. Measurements were done in the setup shown in Figure 2, without the porous outer cylinder. The experiments focused on the measurement of velocity in the cylinder's wake. The measuring line was located in the middle of the cylinder, in the transverse ($y = 0$) and spanwise ($z = 0$) directions. The instantaneous x and y velocities were measured at 36 points along this line, from $x = 0.75 \cdot D_i$ up to $x = 6 \cdot D_i$. The step size was nonuniform to obtain a higher resolution for measuring in the recirculation zone. Instantaneous velocity components were measured during a sampling time of ~200 s, corresponding to about 150 vortex shedding periods.

The goal of the measurements for the cylinder with a porous cover was to validate the numerical work. The geometry of the experimental setup is shown in the left part of Figure 2, and the measuring grid in the right part. Halfway between the inner and the outer cylinder, on a circle with diameter $D_r = D_i + \frac{1}{2}\delta_g$, the tangential velocity component v_τ was measured at various angles Θ from the stagnation point. The radial velocity distribution could not be measured because of the small height of the gap. The measuring points were uniformly distributed, with an angular step size $\Delta\Theta = 15°$.

The flow in the water tunnel was seeded with neutrally buoyant, hollow glass beads (10-μm mean dia.), which penetrated well through the porous material. Laser light was supplied by an argon-ion laser (Model 2016, Spectra Physics Inc.). A TSI Colorburst 9201 beam splitter was used to produce two beam pairs (green: 514.5 nm, and blue: 488.0 nm). For measurements in the wake of the uncovered cylinder, the blue and green beams were used to measure the x and y velocity components, respectively. For the covered cylinder measurements, the green beams were used to measure the tangential velocity component. The beams were coupled through single-mode, polarization-preserving optical fibers to a two-component LDA probe. The probe was operated in backscatter mode for the measurements in the wake of the bare cylinder. The forward-scatter mode, with a reference beam method, was employed for the gap measurements in the covered-cylinder experiments (Drain, 1980). An IFA750 signal analyzer was used to process the real-time signal.

Results and Discussion

This section presents computational and experimental results, and is divided into three subsections. The first concerns fluid flow around a bare cylinder (computational and experimental), the second concerns fluid flow around a sheathed cylinder (computational and experimental), and the third concerns heat and mass transfer to a sheathed cylinder (computational only).

Fluid flow around an uncovered cylinder

First, the fluid flow around an uncovered cylinder was considered. The objective was to find an appropriate turbulence model for the relevant range of Re. As mentioned previously, two two-equation turbulence models have been compared, namely, the standard k-ϵ and RNG k-ϵ models. Predictions from these models have been compared to experimental data from the literature, to LES and DNS simulations from the literature, and to our own present experimental data.

In the literature, most experimental and LES/DNS data have been reported for $Re = 3.9 \cdot 10^3$, which is almost equal to the lower limit of the Re range being considered in the present work. As mentioned, the flow around a cylinder for such a Re number is subcritical and periodical. The predicted time-averaged dimensionless pressure distribution on

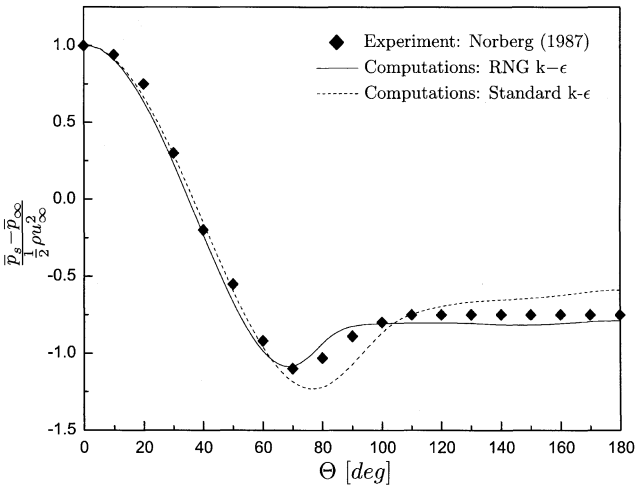

Figure 3. Time-averaged pressure coefficient as a function of angle.

the cylinder surface vs. angle for the standard k-ϵ (S k-ϵ) and RNG k-ϵ (RNG k-ϵ) models is shown in Figure 3. Time-averaged experimental data of Norberg (1987) have been included for validation. The graph shows that both computed pressure distributions are in fair agreement with the experimental data by Norberg, but clearly the curve obtained with RNG k-ϵ fits the experimental data better.

As mentioned previously, in the present LDA experiments, two instantaneous velocity components (v_x and v_y) were measured. The time-averaged value of v_y was found to be close to zero, as expected. Based on the time-resolved values of v_y, the frequency of vortex shedding was estimated. The dimensionless frequency for $Re = 3.9 \cdot 10^3$ to $20 \cdot 10^3$ was $St = 0.20 - 0.22$, which is in good agreement with the values $St = 0.19 - 0.24$, reported by Zdravkovich (1997) for subcritical flow. Using DNS, Ma et al. (2000) found $St = 0.203$, whereas Tremblay (2001) found $St = 0.22$. Breuer (1998) by means of LES found $St = 0.215$.

In order to further verify the present RANS velocity predictions, the computed time-averaged streamwise velocity, v_x, along the center line behind the cylinder has been compared to time-averaged experimental data from present experiments and from the literature (see Figure 4). Ong and Wallace (1996) (O&W) measured the time-averaged streamwise velocity behind a cylinder at $x/D = 3 - 10$. Lourenco and Shih (1994) (L&S) presented time-averaged streamwise velocities along the center line for the near wake [data published in (Beaudan and Moin, 1994)], that is, $x/D = 0.7 - 4.5$. Both data sets have been included in Figure 4, where $x/D = 0$ corresponds to the axis of the cylinder. The length of the recirculation zone, where $\bar{V}/u_\infty \le 0$, as measured by L&S and in the present LDA experiments, is almost the same (about $1D$). Velocities in the region behind the recirculation differ slightly: present measurements show the velocity increasing faster behind the recirculation region. This can be due to different values of the blockage ratio, which is defined as the ratio of the tunnel height over the cylinder diameter ($b = H/D$). For the O&W experiments, the blockage ratio was $b \approx 5$, as compared to $b \approx 4.2$ in the present experiments. The blockage ratio in the experiments by L&S was not reported. In the region behind the recirculation ($2D < x < 4D$), the measurements of O&W show a better agreement with the present work than the L&S experiments. Finally, data computed with LES (Breuer, 1998) and DNS (Tremblay, 2001) were included. These data, together with O&W, are in good agreement with the present experiments in the entire wake region.

The mean center line velocities predicted with the RNG k-ϵ and S k-ϵ models are compared to the experimental and LES data in Figure 4 just mentioned. For both turbulence models, the computed recirculation length is slightly shorter than the measured $1D$, but the prediction with RNG k-ϵ is better than with S k-ϵ ($0.9D$ and $0.7D$, respectively). In both cases the velocity distribution in the recirculation zone is not predicted very well. In the region behind the recirculation ($2D < x < 3D$), the computed velocities are slightly lower than those measured in the present LDA experiments and slightly higher than those measured by L&S. In the wake region ($x > 3D$), the predicted velocities fit both the present measurements and those by O&W.

In Figure 5 the drag coefficient vs. Re, as computed with RNG k-ϵ, has been compared with the experimental data fit given in White (1991). For Re up to $2 \cdot 10^4$, the computed values show very good agreement with the experimental data. For higher Re, the computed drag coefficients are slightly above the experimental curve, but the deviation is still less than 10%.

Based on the comparisons presented in Figures 3 to 5, we conclude that the RNG k-ϵ model predicts the time-averaged flow around a cylinder, for the Re numbers of interest, with acceptable accuracy. For the case of a solid cylinder sheathed by a porous layer, a correct prediction of the turbulent outer flow field will probably lead to a correct prediction of the laminar flow field inside the gap as well. Therefore, in the following sections, the RNG k-ϵ model will be used to calculate flow, heat, and mass transfer around such a sheathed cylinder. The flow simulations will again be compared with experimental data.

Fluid flow around the sheathed cylinder

For the covered cylinder case, computations have been performed for varying Re and $DaIc$, at constant $Ig = 5 \cdot 10^{-2}$.

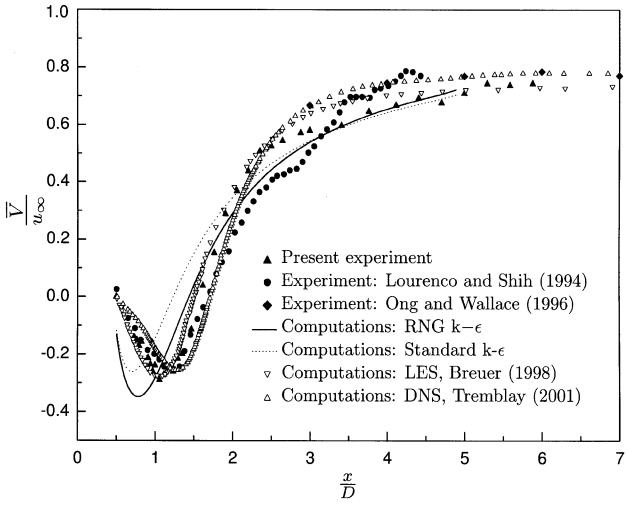

Figure 4. Mean streamwise velocity along the center line.

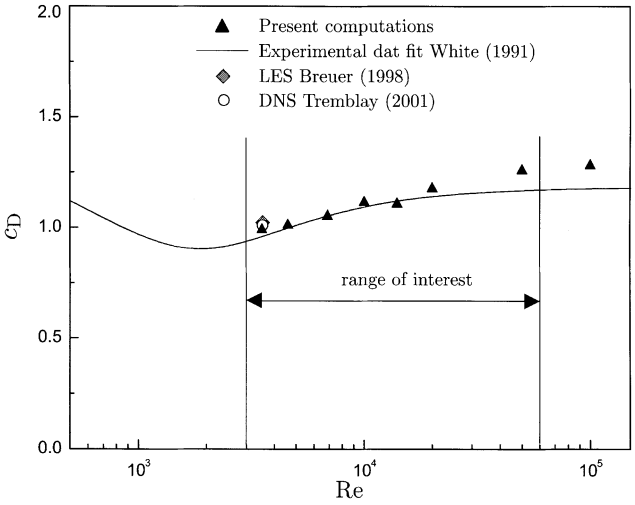

Figure 5. Drag coefficient as a function of the Reynolds number.

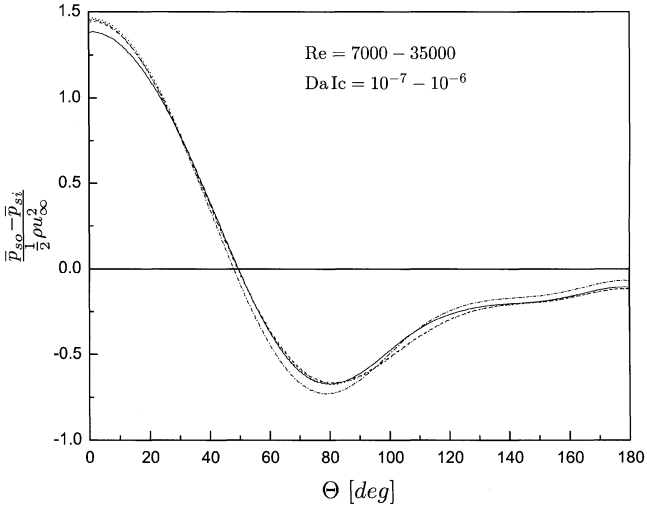

Figure 6. Pressure difference between porous and solid cylinder surface as a function of the angle, for a few different cases ($Re = 7{,}000 - 35{,}000$, $DaIc = 10^{-7} - 10^{-6}$).

The different curves (nearly) coincide, showing the independence on *Re* and *DaIc* in the studied range.

Additionally, the influence of varied *Ig* has been studied. Variation of *Re* has been achieved by changing the free-stream velocity, at fixed geometrical and fluid properties. The *DaIc* changes were obtained by changing the air permeability of the porous material or the thickness of the porous layer.

Figure 6 presents the computed dimensionless time-averaged pressure difference between the outer and inner cylinder surface, as a function of angle. It is found to be virtually independent of both *Re* and *DaIc*. Two regions can be distinguished: the first, where the outer pressure is higher than the inner pressure, and the second, with higher inner pressure. In the first region, air from the outside flows through the porous layer into the air gap, and in the second region, air flows out again. The border between the two regions is located where the pressure-difference curve passes through zero ($\Theta \approx 50°$).

Figure 7 presents the computed tangential velocity component inside the air gap (at a location halfway between the inner and outer cylinder, and scaled with $u_\infty ReDaIc$) as a function of the angle, for various *DaIc* and *Re*. For $\Theta = 0$ and 180°, the tangential velocity component is, of course, zero, whereas a maximal value occurs for $\Theta \approx 50°$. The normalized

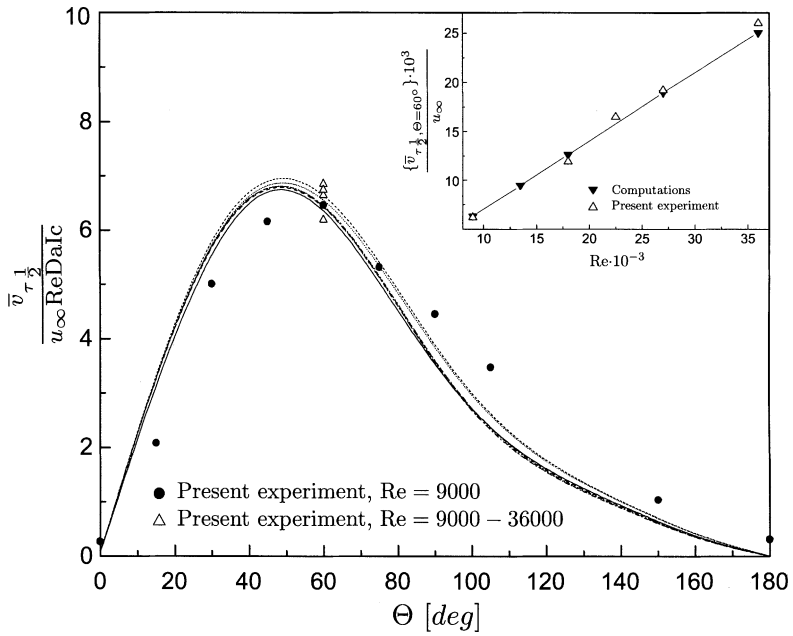

Figure 7. Air-gap velocity as a function of the angle for a set of computational cases ($Re = 7{,}000 - 35{,}000$, $DaIc = 10^{-7} - 10^{-6}$) with experimental data.

The different curves (nearly) coincide, showing the independence on *Re* and *DaIc* in the studied range.

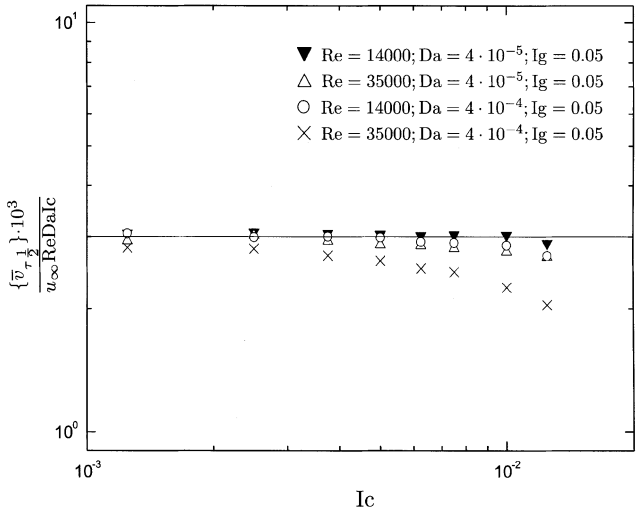

Figure 8. The tangential velocity component underneath the porous cylinder as a function of porous layer thickness.

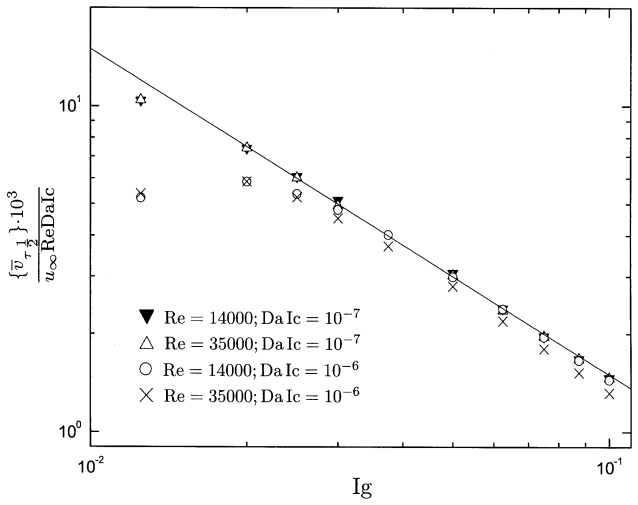

Figure 9. The tangential velocity component underneath the porous cylinder as a function of gap thickness.

velocities scale linearly with *DaIc* and *Re*. Note, that this means that the unscaled velocity underneath the porous cylinder scales with u_∞^2. The same linear correlation between the velocity underneath the porous material and *Da* has been found experimentally by Watanabe et al. (1991).

To further illustrate that $\hat{v} = v/u_\infty$ underneath the porous cylinder scales with *ReDaIc*, as suggested by Eq. 13 and in Figure 7, we have varied *Ic* at various combinations of *Re* and *Da* (see Figure 8). Indeed, for lower values of *Re* and *Da*, $\hat{v}$ scales with *ReDaIc*, since air penetration under these circumstances is limited by the resistance of the porous layer. For higher values of *Re* and *Da*, the friction inside the air gap becomes significant and Eq. 13 no longer holds.

The tangential velocity as a function of the dimensionless air-gap size, *Ig* (that is the dimensionless distance between inner and outer cylinder), is given in Figure 9. The variation in the relative gap size was achieved by changing the diameter of the solid cylinder at a fixed diameter of the porous cylinder. For large gap sizes, air penetration is determined by the resistance of the porous material, and consequently the velocity underneath the porous cylinder is inversely proportional to the gap size. For smaller gap sizes, the air penetration is limited by friction in the gap, and the velocity inside the gap decreases with decreasing air gap thickness.

In the simulations of the flow around a cylinder sheathed by a porous layer, three assumptions were made, which need to be validated: first, that the RNG k-ϵ model accurately models the turbulent flow around a porous cylinder; second, that Darcy's law accurately predicts the flow through the porous layer; and third, that the flow underneath the porous layer is laminar. To this end, LDA experiments of the tangential velocity in the gap between the solid inner cylinder and the porous outer cylinder were performed in the experimental setup presented in Figure 2. It should be noted that in the experimental setup there were actually small deviations from the idealized geometry illustrated in Figure 1, in particular those caused by the fact that the porous layer around the cylinder was not perfectly cylindrical. In our validation study, the experimental geometry was mapped accurately in the simulations. Furthermore, the permeability of the porous layer in the water experiments was unknown, since the swelling of the textile fibers in water caused changes of the permeability. Therefore, we used the permeability to fit the experimental and computed tangential velocities at $\Theta = 60°$.

First, the tangential velocities in the middle of the gap were measured as a function of angle, for fixed $Re = 9{,}000$. These velocities were found to be periodic with approximately the same frequency as the periodic flow around the outer cylinder. Measured velocities were again time averaged over many vortex-shedding periods. After filtering out the periodic component, the measured turbulence intensity was less than 0.5%, which shows the laminar character of the flow inside the gap. The results are presented in Figure 7 (black circles). The computed data show satisfactory agreement with measurements. Small differences may be due to an imperfect geometrical match between experiments and simulations, and because of inaccuracies in locating the LDA measuring volume exactly halfway in the gap. Second, in order to check the dependence of the flow in the gap on the Reynolds number, a single-point measurement of the tangential velocity was performed at $\Theta = 60°$, for $Re = 9{,}000$–$36{,}000$. The results are presented together with computed data in Figure 7 in the dimensionless form scaled with $u_\infty ReDaIc$ (white triangles), and scaled with u_∞ (small graph). A very good agreement is found between experimental and numerical data. Both the experimental and numerical data show a linear dependence on *Re* of the tangential velocity in the gap. This proves the validity of Darcy's law in the range of Reynolds numbers considered.

Heat and mass transfer to a sheathed cylinder

In this section, heat- and mass-transfer correlations are presented for the sheathed cylinder. The heat transfer is driven by the difference between the free stream tempera-

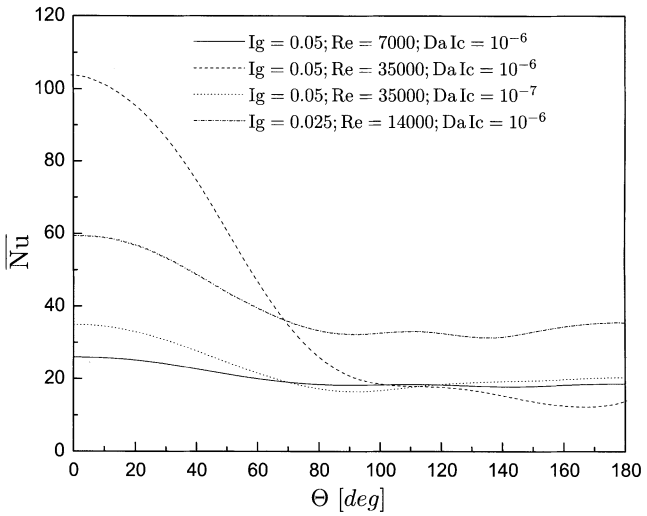

Figure 10. Local Nusselt number as a function of the angle.

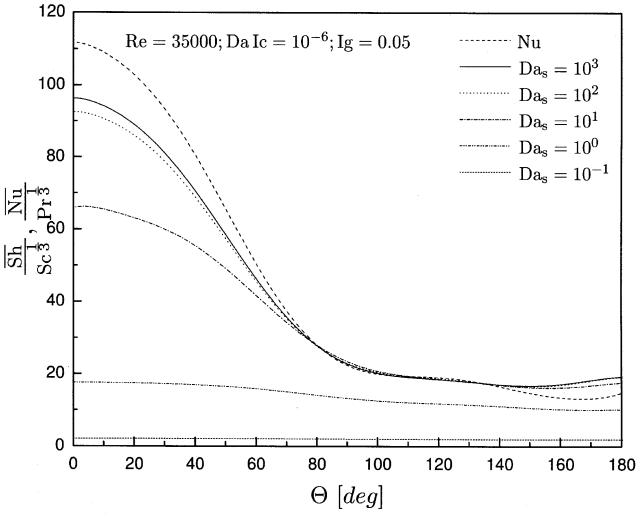

Figure 11. Local Sherwood number vs. angle for different Damköhler numbers.

ture, $T = T_\infty$, and the surface temperature of the cylinder, $T = T_s$, and results in the cooling or heating of the inner cylinder by the outer flow. For the mass-transfer calculations, a trace gas (mass fraction 1%) was added to the air flow. It was assumed that the physical properties of the mixture of air and trace gas were equal to those of air. On the surface of the inner cylinder, the trace gas is adsorbed according to a linear adsorption process. The adsorption rate is related to the Damköhler number (Da_s); $Da_s \to 0$ corresponds to non-adsorbing trace gas, and consequently to a no-flux condition on the inner cylinder surface. $Da_s \to \infty$ corresponds to a very reactive trace gas, which immediately adsorbs on the inner cylinder surface, and consequently a $c = 0$ Dirichlet boundary condition on that surface. In the latter limit, the mass-transfer characteristics are expected to be very similar to the heat-transfer characteristics. Heat- and mass-transfer results will be presented in dimensionless form as Nusselt and Sherwood numbers, respectively, in which the heat flux and mass flux to the cylinder surface were made dimensionless with the free-stream temperature and concentration, the outer cylinder diameter, and the thermal conductivity of the air or the diffusivity of the trace gas, respectively.

Figure 10 presents the calculated time-averaged local Nusselt number distribution for a set of typical values of *Re*, *DaIc*, and *Ig*. For all of the cases analyzed, the maximal value of *Nu*, that is, the most efficient heat transfer, occurs in the neighborhood of the front stagnation point. The front stagnation point heat transfer increases with *Re* and *DaIc*. This is, of course, related to the air velocity inside the gap, which was shown to increase with *Re* and *DaIc* as well. The *Nu* distribution shows that in the back region of the cylinder ($\Theta > 90°$), the heat transfer is determined by conduction in the air gap, that is, the dimensionless thermal boundary-layer thickness in the back region of the cylinder is approximately equal to *Ig*, leading to $\overline{Nu} \approx 1/Ig$.

Figure 11 shows the time-averaged local Sherwood number ($\overline{Sh}$) vs. the angle (Θ), for a few different values of Da_s and fixed *Re*, *DaIc*, and *Ig*. For comparison, the local $\overline{Nu}$ curve is also presented, and $\overline{Sh}$ and $\overline{Nu}$ have been scaled with $Sc^{1/3}$ and $Pr^{1/3}$, respectively. For low Da_s, the mass flux to the inner cylinder surface is limited by the adsorptivity of the trace gas, rather than by flow and diffusion. As a result, the *Sh* number becomes small and uniform. For higher values of Da_s, the shape of the $\overline{Sh}/Sc^{1/3}$ curve is very similar to that of the $\overline{Nu}/Pr^{1/3}$ curve, as is also true for heat and mass transfer to a bare cylinder.

Because of this similarity, only heat transfer was considered in the next study. Figure 12 presents *Nu*, averaged over the time and over the angle, as a function of *Re*, for varied *DaIc* and *Ig*. The white symbols are used for $Ig = 0.05$ (base case), the black ones for $Ig = 0.025$, and the gray ones for $Ig = 0.075$. The experimental curve $\{\overline{Nu_b}\} = f(Re)$ from the literature (Zdravkovich, 1997) for an uncovered cylinder has been added. It can be seen that the average Nusselt number to the sheathed cylinder approaches the value of a bare cylinder when *Re*, *DaIc*, and *Ig* are large. In that case, the air flow easily penetrates the porous sheath, and the latter has little influence on the heat transfer. Similarly, it can be seen that for small *Re* and small *Ig*, the heat transfer is again similar to that for a bare cylinder. In these cases, the boundary layer around the outer cylinder, which now is thicker than the air gap between the cylinders, limits heat transfer. For intermediate values of *DaIc*, *Re*, and *Ig*, the porous sheath can significantly reduce the heat transfer to the inner cylinder. Based on the numerical data presented in Figure 12, the following empirical correlation is proposed

$$\{\overline{Nu}\} = \frac{1}{Ig} + \frac{\alpha \cdot (DaIc)^n \cdot Re^n}{1 + \alpha \cdot (DaIc)^n \cdot Re^n} \cdot \{\overline{Nu_b}\} \quad \text{for} \quad IgRe > 10^3; \quad IgReDaIc < 10^{-2} \qquad (19)$$

where $\alpha = 2.93$, $n = 0.82$, and $\{\overline{Nu_b}\}$ is the Nu number for a bare cylinder.

The results from this correlation are presented in Figure 12 as (dashed) lines, together with the results from numerical simulations (black, white, and gray symbols). In Figure 13, we show a comparison between the Nusselt number predictions from Eq. 19 and the results from a large number of numeri-

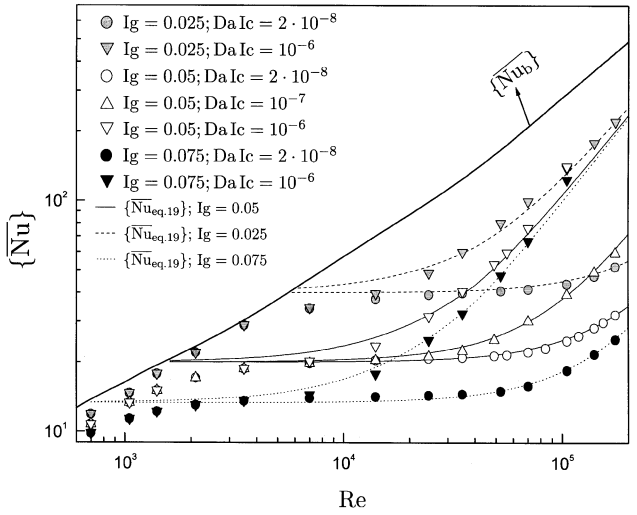

Figure 12. Averaged Nusselt number vs. Reynolds number.

cal simulations for a wide range of conditions ($Re = 7{,}000 - 150{,}000$; $DaIc = 2 \cdot 10^{-8} - 10^{-6}$; $Ig = 0.01 - 0.1$), under the limiting condition that $(IgRe) > 10^3$ and $(IgReDaIc) < 10^{-2}$. Clearly, within the indicated range of validity, Eq. 19 predicts Nusselt numbers for the geometry studied with an accuracy of 5%.

Conclusions

A systematic study of the flow, heat, and mass transfer around a cylinder sheathed by a second, porous cylinder and placed in a perpendicular turbulent air flow has been presented. To this end, 2-D time-averaged flow, heat- and mass-transfer simulations, based on the RNG k-ϵ model, have been performed. Varied parameters were the free-stream Reynolds number, the Darcy number and the dimensionless air resistance of the porous layer, and the dimensionless distance between the outer and inner cylinders. The range of values of the studied parameters was based on applications in heat and mass transfer to a clothed human limb in outdoor wind. The flow simulations were validated against LDA flow measurements for a covered cylinder and against available data from the literature for bare cylinders. For a wide range of conditions, air was found to penetrate the outer porous cylinder in the upstream region, down to an angle of approximately $\Theta = 50°$ from the front stagnation point. In this region, heat and mass transfer are high. Further downstream, heat and mass transfer are dictated by conduction/diffusion through the air layer in between the two cylinders. The dimensionless tangential velocity (scaled with the free stream velocity) underneath the porous cylinder was found to be inversely proportional to the dimensionless resistance *ReDaIc*. Its maximum is also found to be around $\Theta = 50°$. For large Reynolds numbers and small air resistances, the flow easily penetrates the porous sheath and heat transfer approaches that of a bare cylinder. For low Reynolds numbers, on the other hand, the boundary layer around the pair of concentric cylinders becomes very thick and limiting for heat transfer, and again heat transfer approaches that of a bare cylinder. The Nusselt number for heat transfer (and, when the cylinder surface has a high adsorptivity, also the Sherwood number for mass transfer) under a wide range of conditions could be summarized in a single correlation, which is presented as Eq. 19 in this article. Within its range of validity ($IgRe > 10^3$, $IgReDaIc < 10^{-2}$), this correlation is accurate within 5%, compared to the numerical simulations.

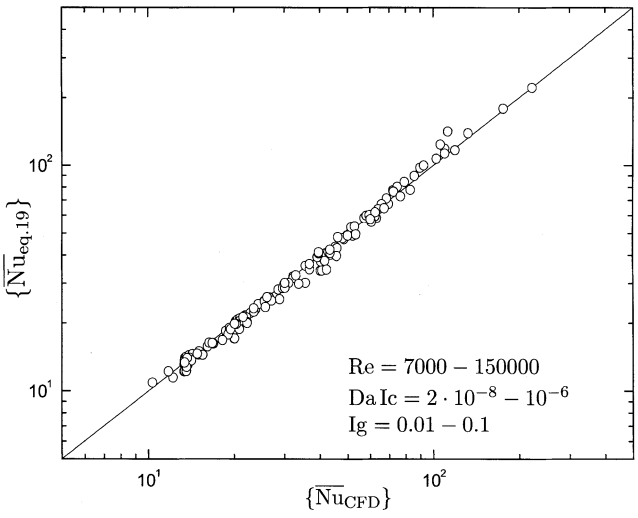

Figure 13. Comparison of proposed theoretical model to CFD data.

Acknowledgment

Research on this project is supported and financed by TNO PML. The authors thank Jaap Beekman for his valuable assistance and advice in the experimental part of this work.

Notation

c = mass fraction
c_D = drag coefficient
c_p = specific heat, $J \cdot kg^{-1} \cdot K^{-1}$
D = diameter, m
$\mathfrak{D}$ = diffusivity, $m^2 \cdot s^{-1}$
Da = Darcy number (see Table 2)
Da_s = Damköhler number (see Table 2)
Ic = porous-thickness ratio (see Table 2)
Ig = air-gap-thickness ratio (see Table 2)
I_t = turbulence intensity
K = permeability, m^2
k_a = adsorptivity, $m \cdot s^{-1}$
L_t = turbulence length scale, m
Nu = Nusselt number = $(q''D)/[(T_s - T_\infty)\lambda]$
P = pressure, Pa
Pr = Prandtl number (see Table 2)
r = radial coordinate, m
Re = Reynolds number (see Table 2)
q'' = heat flux, $W \cdot m^{-2}$
S = source-term vector, $Pa \cdot m^{-1}$
Sc = Schmidt number (see Table 1)
Sh = Sherwood number = $(\phi''D)/(c_\infty \mathfrak{D})$
t = time, s
T = temperature, °C
u_∞ = free-stream velocity, $m \cdot s^{-1}$
v' = fluctuating velocity component, $m \cdot s^{-1}$
V = instantaneous velocity vector, $m \cdot s^{-1}$

x = longitudinal coordinate, m
y = transverse coordinate, m

Greek letters

α = binary parameter
δ_c = porous-medium thickness, m
δ_g = air-gap thickness, m
Θ = angular coordinate, deg
λ = thermal conductivity, $W \cdot m^{-1} \cdot K^{-1}$
μ = dynamic viscosity, $Pa \cdot s$
ρ = density, $kg \cdot m^{-3}$
$\bar{\bar{\tau}}$ = stress tensor, $N \cdot m^{-2}$
ϕ'' = mass flux, $kg \cdot m^{-2} \cdot s^{-1}$

Subscripts

1/2 = midpoint between inner and outer cylinder
∞ = free stream
c = cloth
g = air gap
i = inner
o = outer
s = surface
τ = tangential component

Mathematical symbols

$\overline{\phi}$ = time averaged
$\{\phi\}$ = averaged over the angle (Θ)

Literature Cited

Beaudan, P., and P. Moin, "Numerical Experiments on the Flow Past a Circular Cylinder at Sub-Critical Reynolds Number," *Tech. Rep.*, TF-62, Thermoscience Division, Dept. of Mechanical Engineering, Stanford Univ., Stanford, CA (1994).

Bird, R., W. Stewart, and W. Lightfoot, *Transport Phenomena*, Wiley, New York (2002).

Bo, Q., and T. Nakijama, "Natural and Mixed Convection Around a Cylinder Enclosed with Porous Media—A Numerical Study on Comfort of Clothed Human Being," *Computational Technologies for Fluid/Thermal/Structural/Chemical Systems with Industrial Applications*, Vol. 424-2, C. Kleijn and V. Kudriavtsev, eds., ASME PVP, New York, p. 177 (2001).

Bouskill, L., G. Havenith, K. Kuklane, K. Parsons, and W. Withey, "Relationship Between Clothing Ventilation and Thermal Insulation," *AIHA J.*, **63**, 262 (2002).

Breuer, M., "Large Eddy Simulation of the Subcritical Flow Past a Circular Cylinder: Numerical and Modeling Aspects," *Int. J. Numer. Meth. Fluids*, **28**, 1281 (1998).

Casey, M., and T. Wintergerste, *Quality and Trust in Industrial CFD*, ERCOFTAC-Sulzer Innotec, Winterthur, Switzerland (2000).

Celik, I., and F. Shafer, "Long Time-Averaged Solutions of Turbulent Flow Past a Circular Cylinder," *J. Wind Eng. Ind. Aerodyn.*, **56**, 185 (1995).

Drain, L., *The Laser Doppler Technique*, Wiley, Chichester, UK (1980).

Ferziger, J., and M. Peric, *Computational Methods for Fluid Dynamics*, Springer-Verlag, Berlin (1996).

Fluent Inc., *Fluent 5 User's Guide*, Lebanon, NJ (1998).

Gibson, P., "Review of Numerical Modeling of Convection, Diffusion, and Phase Change in Textiles," *Computational Technologies for Fluid/Thermal/Structural/Chemical Systems with Industrial Applications*, Vol. 397-2, C. Kleijn and S. Kawano, eds., ASME PVP, New York, p. 117 (1999).

Haddad, O., M. Al-Nimr, and M. Abu-Ayyad, "Numerical Simulation of Forced Convection Flow Past a Parabolic Cylinder Embedded in Porous Media," *Int. J. Numer. Method. Heat Fluid Flow*, **12**, 6 (2001).

Holmer, I., H. Nilsson, G. Havenith, and K. Parsons, "Clothing Convective Heat Transfer—Proposal for Improved Prediction in Standards and Models," *Ann. Occup. Hyg.*, **43**, 329 (1999).

Kind, R., C. A. Jenkis, and C. Broughton, "Measurement of Wind-Induced Heat Transfer Through Permeable Cold-Weather Clothing," *Cold Reg. Sci. Technol.*, **23**, 305 (1995).

Lourenco, L., and C. Shih, "Characteristics of the Plane Turbulent Near Wake of a Circular Cylinder, Particle Image Velocimetry Study," published in Tech. Rep. TF-62, Thermoscience Division, Dept. of Mechanical Engineering, Stanford Univ., Stanford, CA (1994).

Ma, X., G.-S. Karmanos, and G. Karniadakis, "Dynamics and Low-Dimensionality of a Turbulent Near Wake," *J. Fluid Mech.*, **410**, 29 (2000).

Norberg, C., "Effects of Reynolds Number and Low-Intensity Freestream Turbulence on the Flow Around a Circular Cylinder," Tech. Rep. 87/2, Dept. of Applied Thermodynamics and Fluid Mechanics, Chalmer Univ. of Technology, Sweden (1987).

Ong, L., and J. Wallace, "The Velocity Field of the Turbulent Very Near Wake of a Circular Cylinder," *Exp. Fluids*, **20**, 441 (1996).

Patankar, S., *Numerical Heat Transfer and Fluid Flow*, Hemisphere, New York (1980).

Sanitjai, S., and R. Goldstein, "Effect of Free Stream Turbulence on Local Mass Transfer from a Circular Cylinder," *Int. J. Heat Mass Transfer*, **44**, 2863 (2001).

Thevenin, J., "Transient Forced Convection Heat Transfer from a Circular Cylinder Embedded in a Porous Medium," *Int. J. Heat Mass Transfer*, **22**, 507 (1995).

Tremblay, F., *Direct and Large-Eddy Simulation of Flow Around a Circular Cylinder at Subcritical Reynolds Numbers*, PhD Thesis, Munich Univ. of Technology, Munich, Germany (2001).

Watanabe, T., T. Kato, and Y. Kamata, "The Velocity Distribution in the Inner Flow Field Around a Clothed Cylinder," *SEN-I GAKKAISHI*, **47**, 271 (1991).

White, F., *Viscous Fluid Flow*, McGraw-Hill, New York (1991).

Zdravkovich, M., *Flow Around Circular Cylinders*, Oxford Univ. Press, Oxford (1997).

Manuscript received Mar. 14, 2003, and revision received May 16, 2003.